A Compensated Open-Loop Impedance Controller Evaluated on the Second-Generation Open-Source Leg Prosthesis

T. Kevin Best , Student Member, IEEE, Gray C. Thomas , Member, IEEE, Senthur R. Ayyappan , Robert D. Gregg , Senior Member, IEEE, and Elliott J. Rouse , Senior Member, IEEE

Abstract—Accurate impedance control is key for biomimetic mechanical behavior in lower-limb robotic prostheses. However, due to compliance, friction, and inertia in the drivetrain, the commonly used open-loop impedance control strategy can often produce inaccurate results without appropriate compensation. This article presents a controller that accounts for these dynamics to improve the impedance rendering accuracy of a robotic prosthesis research platform, the Open-Source Leg (OSL v2). We first develop a dynamic model of the OSL v2's drivetrain and show that it accurately predicts the system's joint torque with 97% mean explained variance across a diverse array of experiments. We then present a controller that compensates for the OSL v2's inherent dynamics using a combination of feedback linearization and actuator-state feedback control. We experimentally validate this controller on the OSL v2 with a rotary dynamometer and in treadmill walking experiments. We show that it can render various constant impedance behaviors with higher stiffness and damping accuracy than a baseline controller. We also show our controller's ability to replicate the variable impedance trajectories of the human ankle joint, suggesting that this control approach could enable robotic prostheses that are biomimetic in their mechanical impedance in addition to their kinematics and kinetics.

Received 28 July 2024; revised 20 September 2024; accepted 21 November 2024. Recommended by Technical Editor L. Cheng and Senior Editor H. Wang. This work was supported in part by National Science Foundation under Grant 1846969, NRI Grant 2024237, and POSE Grant 2229418, and in part by Graduate Research Fellowship under DGE Grant 1841052. (Corresponding author: T. Kevin Best.)

This work involved human subjects or animals in its research. Approval of all ethical and experimental procedures and protocols was granted by Institutional Review Board of the University of Michigan under Application No. HUM00143080.

T. Kevin Best, Senthur R. Ayyappan, and Robert D. Gregg are with the Department of Robotics, University of Michigan, Ann Arbor, MI 48109 USA (e-mail: tkbest@umich.edu).

Gray C. Thomas is with the J. Mike Walker '66 Department of Mechanical Engineering, Texas A&M University, College Station, TX 77840

Elliott J. Rouse is with the Department of Robotics, University of Michigan, Ann Arbor, MI 48109 USA, and also with the Department of Mechanical Engineering, University of Michigan, Ann Arbor, MI 48109 USA (e-mail: ejrouse@umich.edu).

This article has supplementary material provided by the authors and color versions of one or more figures available at https://doi.org/10.1109/TMECH.2024.3508469.

Digital Object Identifier 10.1109/TMECH.2024.3508469

Index Terms—Impedance control, prosthetic limbs, robot control, wearable robots.

I. INTRODUCTION

OWER-LIMB prostheses that restore normative biomechanics have the potential to improve community mobility for people living with amputation. Individuals with amputation often exhibit slower gait speeds [1], increased fall risk [2], lower back pain [3], osteoarthritis [4], and lower community engagement [5] when compared to able-bodied populations. Modern variable-damping prostheses, commonly known as "microprocessor controlled" prostheses, have been shown to increase speed and user confidence compared to mechanical prostheses [6], but are fundamentally limited by their passive nature. Most commercially-available prostheses are unable to provide net-positive energy, and thus cannot fully replace the role of biological muscles to produce the limb mechanics needed for many activities of daily life (e.g., stair ascent) [7], [8]. Thus, powered prostheses have been proposed as an alternative, as their motors could be used to actively supply energy and more closely emulate biological limbs.

Despite their promise, powered prostheses have remained primarily in academia due to the challenge of developing their control strategies, among other factors [9], [10], [11]. While weight, cost, and audible noise are ever-present barriers, the development of successful control strategies is particularly challenging due to the heterogeneous nature of real-world ambulation. The appropriate control actions at any given moment can depend on many highly-variable factors including the terrain and the user's intent. Thus, effective and robust control of robotic prostheses remains a challenge and an active research area [11].

The Open-Source Leg (OSL) project aims to address this challenge by enabling academic researchers to investigate control strategies for robotic prostheses on a common hardware and software platform [12]. The newly developed second generation OSL (OSL v2) is a robotic knee-ankle prosthesis that was designed to assist researchers by easing the burden to manufacture, assemble, and control the prosthesis. The system is comprised of off-the-shelf actuation and easily manufactured components, with fully open-source design files and software available to the research community [13]. As an openly designed

robotic prosthesis, the OSL v2 allows researchers to focus their efforts on developing novel and transformative solutions for control without having to first design their own hardware from scratch.

Impedance control is a common strategy used in lower-limb prostheses to create mechanical behaviors that emulate human walking [9], [10], [11], [12], [14], [15], [16], [17], [18], [19], [20], [21], [22], [23]. It is a middle-ground between kinematic control and force/torque control, where the desired joint torque is calculated to emulate a spring-damper system with a joint stiffness K, viscous damping B, and equilibrium angle θ_{eq} . Many impedance controllers operate in open-loop, meaning that the output torque at the joint is not directly measured and used for feedback [9], [10], [12], [16], [17], [18], [19], [20], [21], [22], [23]. In practice, many open-loop impedance controllers assume a proportional relationship between the joint torque and the motor current, neglecting the effects of transmission elasticity, friction, and inertia [12], [16], [18], [19], [20], [22], [23], [24], [25], [26]. While this assumption has been shown to be valid for some hardware with low transmission ratios (e.g., [18]), previous work on the OSL v2's hardware showed that significant drivetrain dynamics can exist even for a motor with a low gear ratio [27]. These dynamics caused an open-loop impedance controller that assumed proportionality between motor current and joint torque to produce inaccurate impedance rendering, particularly as the transmission ratio of the actuator was increased. These findings indicate that, even for simple, low-ratio drivetrains, open-loop impedance control without compensation may be insufficient to render accurate joint dynamics.

Historically, two primary approaches have been used to improve the output impedance accuracy of a robot, including prostheses. The first is to simply implement closed-loop impedance control (i.e., adding a sensor to directly measure output torque). This can be achieved, e.g., using a load cell as in [14] or a series elastic actuator (SEA) as in [28], [29], [30], and [31]. However, concerns regarding mass, cost, volume, and control bandwidth often accompany this approach. Another approach is to use parameterized models of the system's dynamics along with feedback controllers to cancel or otherwise modify the unwanted aspects of the system's behavior. This approach has been successfully used for low-frequency inertia compensation [32] and friction compensation [28], [33], [34]. However, model-based compensation requires accurate estimates of the model parameters and can suffer from instability due to model errors, particularly when attempting to compensate for inertia.

In this article, we present a control strategy for the OSL v2 that improves its ability to accurately render a desired joint impedance, parameterized by stiffness and damping. We build upon our previous work [27], which suggested a linear map to improve the impedance rendering of the actuator alone, by proposing a model-based compensation strategy for the full OSL v2 drivetrain. We first show that the OSL v2's actuator and belt-drive transmission display inertial, dissipative, and nonlinear elastic behaviors, and we provide a model that describes these behaviors with high accuracy. We use this model with a combination of feedback linearization and actuator-state feedback control to modify the system dynamics and improve

the accuracy of the OSL v2's mechanical impedance rendering. We then validate our controller by experimentally characterizing the OSL v2's rendered impedance on a rotary dynamometer, demonstrating a substantial improvement in accuracy when compared to a baseline uncompensated controller. We also show that our controller can render the impedance trajectories of the human ankle joint during walking [35], [36], [37], [38], enabling the future development of prosthesis controllers that could provide biologically appropriate mechanical impedance, in addition to providing biomimetic kinetics and kinematics during locomotion. Our specific contributions are as follows:

- an overview of the second-generation Open-Source Leg's design and capabilities;
- a parametric model of the OSL v2's drivetrain dynamics, which predicted the output joint torque within an average of 5.2% of peak values and demonstrated a 97% mean variance accounted for (VAF) across dynamometer experiments;
- a novel application of feedback linearization and actuatorstate feedback control that accounts for the undesired drivetrain dynamics and improves the accuracy of the OSL v2's mechanical impedance rendering;
- 4) a thorough validation of the proposed impedance control method, quantifying its performance improvements relative to a baseline uncompensated controller during both dynamometer and treadmill walking experiments.

Our goal was to advance a method to enable accurate impedance control for the OSL community [12], [20], [26], [39], [40], [41], [42] and for other robotic systems with similar architectures. By providing a common high-performance hardware and control ecosystem, we aim to help accelerate the development of new control solutions for robotic leg prostheses.

II. SECOND-GENERATION OPEN SOURCE LEG

The second-generation Open-Source Leg (OSL v2, Fig. 1) is a novel iteration of the first-generation OSL, presented in [12] and [43]. As this is the first publication using the OSL v2, this section provides an overview of its updated hardware design and the notable changes from its predecessor. These changes, which were largely informed by feedback from the OSL community, focused on reducing the system's complexity with fewer custom-machined parts, making the OSL more portable and self-contained to facilitate research experiments outside laboratory environments, and enhancing the system's technical abilities by improving the hardware design and the options for researcher-specific customization.

During the redesign process, we favored new designs comprising more off-the-shelf components to reduce hardware costs (~\$19000) and to simplify the assembly process relative to the OSL v1. Our chosen design features off-the-shelf battery packs (Dephy BA30, Boxborough, MA, USA), improving safety and eliminating the need for additional battery management systems. The knee and ankle joints feature identical drivetrains, consisting of a quasi-direct drive actuator that comprises an exterior rotor brushless motor and an integrated 9:1 planetary gear reduction (Dephy ActPack 4.1, Boxborough, MA, USA based on the



Fig. 1. CAD rendering of the second-generation Open-Source Leg (OSL v2) next to a wire-frame model highlighting its drivetrain and control components. From this view, one can see the identical construction of the knee (a) and ankle (b) joint drivetrains, consisting of an actuator module (c) and a single-stage belt-drive transmission (d). An idler pulley on an eccentric shaft (e) provides tunable belt tension. Batteries with an integrated management system (f) power the actuators and the integrated single-board computer (g). Additional renderings are available in the supplemental material.

T-motor AK80-9, Nanchang, Jiangxi, China), and a single-stage belt transmission with an 4.61:1 reduction (Powergrip GT3 45mm width, Gates, Denver, CO). The design recommends 3mm pitch belts, but includes an option to be assembled with 5mm pitch belts; these belts are stiffer but have greater output impedance. The identical construction between the knee and ankle subsystems allows for part sharing and simplifies the low-level control problem, enabling the same characterization, model, and control to be applied to both.

The actuator and transmission components were sized to provide sufficient peak torque capacity (~ 160 Nm for 10 s) to enable research into various ambulation activities. The only differences between the knee and ankle joints are their ranges of motion, which are $[0^{\circ}, 120^{\circ}]$ and $[-30^{\circ}, 30^{\circ}]$, respectively. The ankle's range of motion of 60° is a significant improvement over the OSL v1's ankle range of $[-15^{\circ}, 15^{\circ}]$. This facilitates the use of the OSL v2 for various activities involving stairs and ramps more effectively. The OSL v2 is also compatible with two foot options: 1) the Variflex LP (Össur, Reykjavík, Iceland); and 2) a stiff, low-profile fiberglass foot. The Variflex provides a compliant ground interaction that users are likely used to, while the fiberglass foot provides lower build heights and gives the researcher more control over the ankle mechanics. In this work, we use the fiberglass foot.

Other notable changes from the original OSL include new housings (7075-T6 aluminum), which provide for a minimum build height of 451mm and a total assembled mass (knee-ankle) of 5.4 kg including the batteries and electronics. This makes the OSL v2 a fully self-contained system that can be used to conduct research experiments outside of a traditional laboratory setting. We also created a new belt tensioning system with an idler pulley that rotates about an eccentric shaft, which can

be adjusted in increments of 5° to tension the belt. This new tensioning system is easier, faster, and more precise. Finally, the hardware, electronics, and software library were all intentionally designed to be modular, allowing the OSL v2 to be used in various configurations depending on the researchers' needs (e.g., knee only operation).

The OSL v2's control logic is executed at 300 Hz on a single-board computer (Raspberry Pi 4B+, Cambridge, U.K.) integrated into the knee housing. The standard sensor suite includes motor encoders, joint encoders, and a 6-axis load cell mounted midshank (see [12] for full detail), though more sensors can be added. Low-level motor control loops are executed on the actuators themselves, with impedance or position control operating at 1 kHz and current control operating at 10 kHz. For more information on the OSL v2, its capabilities, design, and software tools, please see the project's website (www.opensourceleg.org).

III. JOINT IMPEDANCE CONTROLLER

As we discussed in the introduction, the accuracy of an openloop impedance controller can be improved through knowledge of and compensation for the system's inherent dynamics. In this section, we develop a dynamic model of the OSL v2 drivetrain and present a feedback controller to improve the output impedance. Note that while our experiments focus on the ankle joint, the same characterization and control approach can be applied to the knee joint, as they are mechanically identical.

A. Drivetrain Model

1) Actuator: Due to its popularity in wearable robotics, the OSL v2's actuator has been characterized previously [27], [44]. Nesler et al. present a model in which the actuator's output torque $\tau_{\rm a}$ is described by

$$\tau_{\rm a} = \tau_{\rm m} - \tau_{\rm f}(\dot{\theta}_{\rm a}, I_q) - B_{\rm a}\dot{\theta}_{\rm a} - J_{\rm a}\ddot{\theta}_{\rm a} \tag{1}$$

where $\tau_{\rm m}=I_qk_tn_{\rm a}$ is the motor output torque produced by the q-axis motor current I_q , the corresponding torque constant k_t , and the actuator's gear ratio $n_{\rm a}$. $B_{\rm a}$ represents viscous losses due to the actuator velocity $\dot{\theta}_{\rm a}$, and $J_{\rm a}$ captures the combined effects of rotor and gearbox inertial torques due to the actuator's acceleration $\ddot{\theta}_{\rm a}$. Finally, the friction losses $\tau_{\rm f}(\dot{\theta}_{\rm a},I_q)$ are defined

$$\tau_{\rm f}(\dot{\theta}_{\rm a}, I_q) = \operatorname{sgn}(\dot{\theta}_{\rm a}) \left(f_c + f_g |I_q| \right) \tag{2}$$

where f_c and f_g parameterize coulomb and gear friction, respectively.

To identify the model parameters, we ran benchtop experiments with two actuators opposing one another and connected via a contactless torque sensor (TRS605, FUTEK, California, USA), similar to the experiments in [27], [44], and [45]. We commanded steady-state pairs of voltage v and current i to each motor for five seconds, taken from a grid defined as $v \in [-40, 40]$ V, $i \in [-17.5, 17.5]$ A. We then performed a second, nonsteady-state experiment to identify inertia, in which one actuator performed a series of sinusoidal velocity profiles and the other commanded zero current. In each experiment, the torque at the actuator output was measured by a load cell, along with the actuator current and position.

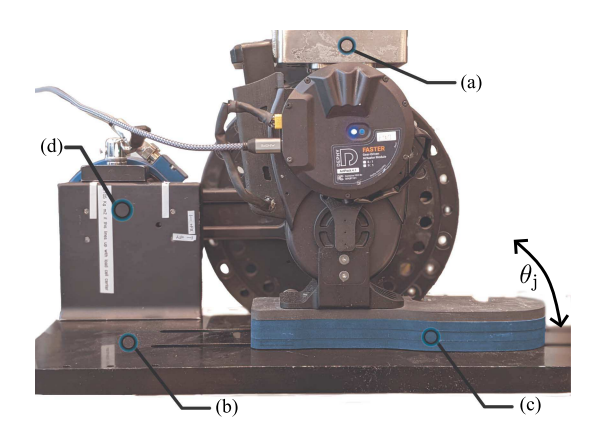


Fig. 2. Annotated photo of the OSL v2 ankle mounted in the dynamometer. The OSL v2 shank is mounted to the dynamometer's static base (a) and the foot is mounted to its motion platform (b), which controls the joint angle $\theta_{\rm j}$. A rigid spacer (c) is used beneath the OSL v2's foot in order to align the ankle axis with the dynamometer's rotation. A load cell (d) measures the reaction torque produced by the motion.

We regressed the torque and actuator data and found that the specific parameters of the actuator model are $k_t=110.8\times 10^{-3}$ Nm/A, $J_{\rm a}=9.83\times 10^{-3}$ kg m², $B_{\rm a}=6.06\times 10^{-2}$ Nms/rad, $f_c=17.1\times 10^{-2}$ Nm, and $f_g=82.1\times 10^{-3}$ Nm/A. The variance accounted for by the model was 99.7% and the RMS residual was 3.0% of the peak torque, indicating that the model accurately captured the actuator dynamics. If we only include the term proportional to current in the model, the normalized RMS residual increases to 6.5%. Thus, the remaining terms are important to include, as they reduce the average model error by over 50%.

2) Transmission: The actuator's output is connected to the OSL v2's single-stage belt-drive transmission. Initial testing showed that the belt is slightly elastic and it thus introduces a passive compliance to the drivetrain dynamics that is similar to an SEA. We modeled and characterized this compliance in order to appropriately account for it in the controller design. We relate the actuator output angle θ_a to the joint angle θ_j via the transmission's effective angular deflection θ_s as

$$\theta_{\rm j} = \frac{\theta_{\rm a}}{n_{\rm t}} + \theta_{\rm s} \tag{3}$$

where $n_{\rm t}$ is the transmission's gear ratio.

Using a rotary dynamometer (motor: Baldor BSM90N-3150AF; load cell: JR3 45E15A4), we performed an experiment to investigate how θ_s related to the torque in the transmission τ_s . With the OSL v2's shank rigidly mounted, we used the dynamometer to control the ankle joint position and to measure the subsequent reaction torque (see Fig. 2). Note that the inertial properties of the dynamometer's mounting hardware were characterized and their contributions to the measured joint torque were subtracted from the measurements prior to the analysis. With the actuator position controlled to zero displacement, the dynamometer drove the joint angle at a slow, constant rate from 0.0 to 0.167 rad while the actuator angle, joint angle, and joint torque were recorded. The experiment was repeated ten times to reduce variance and to test for repeatability. A consistent torque-deflection curve emerged (Fig. 3), and we regressed a

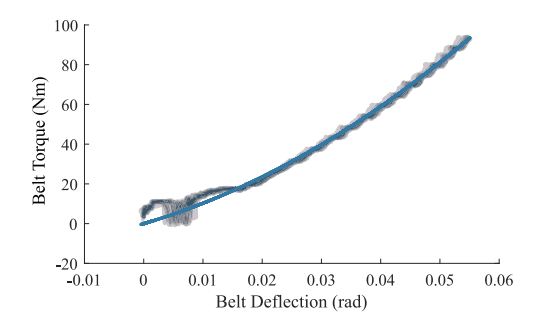


Fig. 3. Loading portion of the drivetrain belt's torque-deflection curve under positive displacement. The dark transparent lines depict each of the ten repeated trials. The blue solid line shows the best fit quadratic function $\rho(\theta_{\rm s}) = p_2\theta_{\rm s}^2 + p_1\theta_{\rm s}$, where $p_2 = 14913$ and $p_1 = 876$.

quadratic function $\rho(\theta_s) = p_2\theta_s^2 + p_1\theta_s$, defined for $\theta_s \in \mathbb{R}^+$, to the data with $R^2 = 0.997$. These results suggest that the belt in the transmission acts as a nonlinear spring, with stiffness increasing linearly with deflection. While a simpler model with a constant stiffness may be preferable, it can be shown that ignoring the belt's stiffening behavior can result in steady-state torque and impedance errors of up to 20% during large torque conditions. We further note that there appears to be a minor backlash behavior around zero deflection, but choose to neglect it for model simplicity.

Experiments with negative belt deflections yielded similar results, allowing us to write an expression for the torque applied at the ankle joint as a function of the belt deflection over a full domain $\theta_s \in \mathbb{R}$ as

$$\tau_{\rm j} = -\tau_{\rm s} = -\operatorname{sgn}(\theta_{\rm s})\rho(|\theta_{\rm s}|).$$
 (4)

We can likewise model the belt's local stiffness $K_{\rm s}$ as a function of $\theta_{\rm s}$ as

$$K_{\rm s}(\theta_{\rm s}) = \frac{d\rho(\theta_{\rm s})}{d\theta_{\rm s}} = 2p_2|\theta_{\rm s}| + p_1. \tag{5}$$

The motor dynamics (1), the kinematic deflection relationship (3), and the belt torque/deflection model (4) collectively define our dynamic model of the OSL v2 drivetrain, relating the input torque produced by the motor current I_q to the torque applied at the joint τ_j . The joint torque acts on the foot's inertia J_f , and the overall motion of the system is determined by τ_j , J_f , and any ground reaction torques applied to the foot τ_{grf} . We summarize these dynamics graphically as a translational system in Fig. 4.

B. Controller Design

Utilizing the knowledge of the OSL v2's drivetrain dynamics, we aim to design a controller that can more accurately render a desired joint impedance compared to an uncompensated open-loop controller. Particularly, we want $\tau_{\rm j}$ to obey an impedance law of the form $\tau_{\rm j}^{\rm des}=-K_d(\theta_{\rm j}-\theta_{\rm eq})-B_d\dot{\theta}_{\rm j},$ where K_d and B_d are the desired joint stiffness and damping, respectively. For conciseness in this section, we will only explicitly consider the case where $\theta_{\rm eq}=0.$ In practice however, any arbitrary $\theta_{\rm eq}$ can be accommodated through a change of variables (i.e., $\theta_{\rm j}=\hat{\theta}_{\rm j}-\theta_{\rm eq})$ without loss of generality.

We utilize a combination of feedback linearization and actuator-state feedback control, similar to [46] and [47]. First,

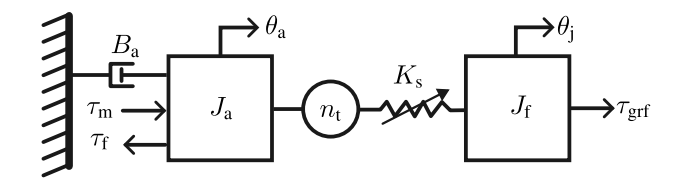


Fig. 4. Schematic of the OSL v2 drivetrain model, depicted as a translational model for clarity. The motor output torque $\tau_{\rm m}=I_qk_tn_{\rm a}$ is opposed by actuator friction $\tau_{\rm f}$ and viscous damping $B_{\rm a}.$ The net torque acts on the actuator inertia $J_{\rm a}.$ The actuator angle $\theta_{\rm a}$ is reduced through the transmission ratio of the belt-drive $n_{\rm t}$ and connected to the output port $\theta_{\rm j}$ via a variable stiffness spring. The spring, with a local stiffness $K_{\rm s}(\theta_{\rm s})$ defined in (5), accounts for the compliance of the belt-driven transmission, which changes linearly with belt deflection $\theta_{\rm s}.$ The resulting joint torque $\tau_{\rm j}$ acts on the inertia of the foot $J_{\rm f},$ whose motion is determined via $\tau_{\rm j}$ and any externally applied torques from the environment $\tau_{\rm crif}.$

we discuss a friction compensation method that results in linear motor dynamics. Using these linearized dynamics, we then derive a feedback control law around the actuator states that optimally renders the desired impedance based on a frequency domain analysis.

1) Friction Compensation: The actuator model regressed in Section III-A1 produced RMS output torque residuals under 0.65 Nm and a high VAF of 99.7%. We therefore are sufficiently confident in the fidelity of the model to use feedback of the actuator's state to linearize its dynamics. Through algebraic manipulation of (1) and (2) (see Appendix A1 for a full derivation), we can select a motor current I_q to cancel friction effects based on a desired actuator output torque $\tau_{\rm a}^{\rm des}$

$$I_q = \frac{\tau_{\mathbf{a}}^{\mathsf{des}} + \mathsf{sgn}(\dot{\theta}_{\mathbf{a}}) f_c}{k_t n_{\mathbf{a}} - \mathsf{sgn}(\tau_{\mathbf{a}}^{\mathsf{des}} \dot{\theta}_{\mathbf{a}} + |\dot{\theta}_{\mathbf{a}}| f_c) f_q}.$$
 (6)

Substituting (6) into (1) and (2) and assuming a perfect friction model, the torque at the output of the actuator becomes a linear function in the desired actuator output torque: $\tau_{\rm a} = \tau_{\rm a}^{\rm des} - B_{\rm a}\dot{\theta}_{\rm a} - J_{\rm a}\ddot{\theta}_{\rm a}$. The actuator torque and the joint torque are related by $\tau_{\rm j} = n_{\rm t}\tau_{\rm a}$. Thus, the torque at the joint is given by

$$\tau_{\rm j} = n_{\rm t} \left(\tau_{\rm a}^{\rm des} - B_{\rm a} \dot{\theta}_{\rm a} - J_{\rm a} \ddot{\theta}_{\rm a} \right). \tag{7}$$

2) Actuator-State Feedback Controller: We select a feedback control law for the actuator based on its angular position and velocity

$$\tau_a^{\text{des}} = K_1(\theta_{\text{a.eq}} + \theta_a^* - \theta_a) - B_1 \dot{\theta}_a \tag{8}$$

where K_1 and B_1 are feedback gains. We include a bias angle $\theta_{\rm a}^*$, which will be used compensate for the belt transmission's nonlinear spring behavior in the subsequent analysis. Again, we can eliminate the equilibrium angle $\theta_{\rm a,eq}$ through a change of variables without loss of generality. We choose to use only the actuator's states for feedback control, as noncollocated feedback (i.e., using the joint states in (8) directly) poses stability risks in a series-elastic system [48] and extra care must be taken to bound the feedback gains in real systems with time delays and numerically calculated derivatives [49].

First, we select the gain K_1 and the offset angle θ_a^* such that the system produces the desired behavior at steady state (i.e.,

 $\dot{\theta}_{\rm a} \equiv 0$ and $\dot{\theta}_{\rm j} \equiv 0$). That is, we desire the equality condition $\tau_{\rm j} = \tau_{\rm i}^{\rm des} \iff -K_d \theta_{\rm j} = -n_{\rm t} K_1(\theta_{\rm a} - \theta_{\rm a}^*). \tag{9}$

Taking the derivative of (9) with respect to θ_j , we can eliminate one of the two unknown parameters

$$-K_d = -n_t K_1 \frac{\partial \theta_a}{\partial \theta_i}.$$
 (10)

If the transmission belt behaved as a traditional linear spring, solving (10) for K_1 would simply amount to solving a harmonic sum for series springs, and θ_a^* would be zero. However, due to the belt's nonlinearity, we must explicitly calculate $\frac{\partial \theta_a}{\partial \theta_j}$. Recall that $\theta_a = n_t(\theta_j - \theta_s)$. Therefore,

$$\frac{\partial \theta_{\rm a}}{\partial \theta_{\rm j}} = n_{\rm t} \left(1 - \frac{\partial \theta_{\rm s}}{\partial \theta_{\rm j}} \right). \tag{11}$$

Using (4), we can estimate θ_s at a given output torque τ_j via the inverse relationship $\rho^{-1}: \tau_j \in \mathbb{R} \to \theta_s \in \mathbb{R}$ as

$$\theta_{\rm s} = \rho^{-1}(\tau_{\rm j}) = -\operatorname{sgn}(\tau_{\rm j}) \frac{-p_1 + \sqrt{p_1^2 + 4p_2|\tau_{\rm j}|}}{2p_2}.$$
 (12)

As the curvature in Fig. 3 is low, a linear approximation of ρ^{-1} provides a good estimate of its local behavior about a nominal point τ_0 . The first order approximation is

$$\theta_{\rm s} \approx \rho^{-1}(\tau_0) + \frac{d\rho^{-1}}{d\tau_{\rm i}} \Big|_{\tau_{\rm i} = \tau_0} (\tau_{\rm j} - \tau_0).$$
 (13)

We note from (5) that the term $\frac{d\rho^{-1}}{d\tau_{\rm j}}\Big|_{\tau_{\rm j}=\tau_0}=-1/K_{\rm s}(\theta_{\rm s,0})$, which is simply the belt's local compliance at the nominal torque τ_0 and corresponding deflection $\theta_{\rm s,0}$. In practice, we can use the OSL v2's joint encoder to measure $\theta_{\rm j}$ and to calculate τ_0 as $\tau_0=-K_d\theta_{\rm j}$. Because our control code executes much faster than the dynamics of walking, this first-order approximation is sufficient in practice. The derivative of (13) with respect to $\theta_{\rm j}$ is

$$\frac{\partial \theta_{\rm s}}{\partial \theta_{\rm j}} \approx \frac{-1}{K_{\rm s}} \frac{\partial \tau_{\rm j}}{\partial \theta_{\rm j}}.$$
 (14)

Assuming that (9) is true, we can substitute for τ_j to find the following relationship:¹

$$\frac{\partial \theta_{\rm s}}{\partial \theta_{\rm i}} \approx \frac{K_d}{K_s}.\tag{15}$$

Substituting back into (11) and subsequently into (10), we can solve for K_1 as

$$\frac{K_d}{n_t K_1} = n_t - n_t \frac{K_d}{K_s} \Rightarrow K_1 = \frac{K_d K_s}{n_t^2 (K_s - K_d)}.$$
 (16)

With K_1 selected, we can choose θ_a^* to ensure that (9) is satisfied based on (16) and the θ_s approximation from (13). Straightforward algebra (see Appendix A2) produces the following expression for the bias angle:

$$\theta_{\rm a}^* = -n_{\rm t} \left(\frac{\tau_0}{K_s} + \rho^{-1}(\tau_0) \right).$$
 (17)

To specify the remaining gain for the velocity state B_1 , we again use the assumption that, locally around a given operating point,

 1 It can be noted that (15) is the same relationship that one would derive if the belt behaved as a linear spring with a constant stiffness. This analysis highlights the fact that locally around a given deflection, the process of selecting K_1 can be thought of as solving the harmonic sum of a series spring with the local spring content.

a linear approximation of the belt's torque-deflection behavior is sufficient. That is, we assume that the belt behaves as a spring with constant stiffness and thus we can write the closed loop dynamics of the system in the frequency domain at any given time point as

$$\begin{cases} \theta_{\rm j} &= \theta_{\rm a}/n_{\rm t} + \theta_{\rm s}, \\ \tau_{\rm j} &= -K_{\rm s}\theta_{\rm s}, \\ \tau_{\rm a} &= -\left(K_1 + B_1 s + J_{\rm a} s^2\right)\theta_{\rm a}. \end{cases}$$
(18)

The joint's integral admittance is given by the closed-loop transfer function $Y(s) = -\theta_{\rm j}/\tau_{\rm j}$, and the desired integral admittance of the system is given by $Y_d(s) = 1/(K_d + B_d s)$. We prefer to work with integral admittance rather than impedance, as the transfer function $Y_d(s)$ is strictly proper and therefore causal. Algebraic manipulation of the closed-loop dynamics (18) under the assumption of a locally-constant belt stiffness yields

$$Y(s) = \frac{J_{\rm a}s^2 + (B_{\rm 1} + B_{\rm a})s + K_{\rm 1} + K_s/n_{\rm t}^2}{K_s(J_{\rm a}s^2 + (B_{\rm 1} + B_{\rm a})s + K_{\rm 1})}.$$
 (19)

Let $\tilde{Y}(s)$ be the error transfer function (i.e., $\tilde{Y}(s) = Y(s) - Y_d(s)$) and let W(s) be a low-pass filter (third order butterworth, cutoff of 1 Hz) used to discount higher frequency errors. We select B_1 from the domain $\mathcal{B} = \{B_1 | B_1 \geq 0\}$ as

$$B_1^* = \underset{B_1 \in \mathcal{B}}{\arg \min} \ ||W(s)\tilde{Y}(s)||_2^2$$
 (20)

thus finding the value of B_1 that makes our system's behavior as close as possible to that of the desired.

As the local belt stiffness K_s changes with loading, the optimal B_1 likewise changes. Therefore, we created a lookup table containing the solutions to (20) for a grid of possible values for τ_0 , K_d , and B_d , which we calculate offline in MATLAB (fmincon using the interior point method, R2023a). We use linear interpolation for values between lookup table entries. Although this objective function is likely nonconvex, an initial condition of $B_1^0=0.5$ always produced a suitable solution in the allowed domain for all tested conditions, though no formal guarantees are given. Future work will investigate alternative formulations of this optimization that are more suitable for online solution without a lookup table, such as a closed form solution or a convex approximation.

IV. EXPERIMENTAL VALIDATION

We conducted three sets of experiments on the OSL v2 with our proposed controller (C_1) to validate its ability to render desired joint impedance values and trajectories and to compare its performance to an uncompensated baseline controller (C_0) . In the first two experiments, the full lower half of the OSL v2 from the shank downward was mounted in the dynamometer (Fig. 2), allowing us to test the performance of the fully assembled system. We did not individually test the knee joint on the dynamometer, as its identical mechanical construction to the ankle joint would make knee-specific experiments redundant. In a final experiment, we asked a participant with an above-knee amputation to walk with the OSL v2 on a treadmill with each controller in order to test the full system in its intended use case.

We implemented C_0 using a basic impedance control strategy that neglected drivetrain dynamics, simply commanding the

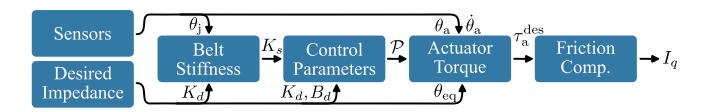


Fig. 5. Control flow diagram indicating the mapping from sensor readings and desired impedance references to a commanded motor current I_q . The expected transmission stiffness $K_{\rm s}$ is calculated using the transmission spring model ρ^{-1} and (5) based on the expected joint torque τ_0 , calculated from the joint encoder measurement $\theta_{\rm j}$ and the desired stiffness K_d . The feedback parameters $\mathcal{P}=\{K_1,B_1,\theta_{\rm s}^*\}$ are calculated from the desired impedance and $K_{\rm s}$ using the equations in Section III-B. These parameters, along with an equilibrium angle $\theta_{\rm eq}$, define a desired actuator torque $\tau_{\rm a}^{\rm des}$ via (8), which is converted to a desired motor current I_q via the friction compensation (6).

motor current based on the desired impedance appropriately scaled by the gear ratios

$$I_{q} = \frac{K_{d}(\theta_{eq} - \theta_{j}) - B_{d}\dot{\theta}_{j}}{k_{t}(n_{a}n_{t})^{2}}.$$
 (21)

We also implemented our new controller C_1 using the theory detailed in Section III-B to account for friction and the drivetrain's dynamics. The control flow diagram in Fig. 5 summarizes the calculation of a desired motor current I_q based on the desired impedance and the system state. At each loop iteration, we used the measured output angle θ_i from the OSL v2's joint encoder to calculate the expected joint torque τ_0 based on the desired stiffness as $\tau_0 = K_d(\theta_{eq} - \theta_j)$. We used the resulting τ_0 to calculate the expected deflection via ρ^{-1} and the corresponding local transmission stiffness K_s using (5). Then, we determined the actuator-state control parameters $\mathcal{P} = \{K_1, B_1, \theta_a^*\}$ by evaluating (16), (17), and (20), respectively. These parameters define a desired actuator output torque $\tau_{\rm a}^{\rm des}$ via (8). Finally, we used the friction compensation (6) to calculate the appropriate I_q to produce $\tau_{\rm a}^{\rm des}$ at the actuator output. To prevent limit cycles that could be caused by the discontinuous zero crossing in the friction model, we smoothly approximated the sign functions by $\sigma(x): x \in \mathbb{R} \to (-1,1)$, given by $\sigma(x) = \frac{x}{\operatorname{abs}(x) + \alpha}$, where $\alpha = 5 \times 10^{-2}$ is a smoothing factor affecting the shape of the zero-crossing.

A. Constant-Impedance Experiments

1) Methods: We first performed a set of dynamic validation trials with each controller over a grid of desired joint impedance values with $\theta_{\rm eq}$ set to 0.0 rad. We conducted one trial for each combination of $K_d \in \{100, 200, 300, 400, 500\}$ Nm/rad and $B_d \in \{1, 3, 5, 7, 9\}$ Nms/rad, which span the typical ranges of stiffness and damping used in impedance controllers. In each trial, the dynamometer drove the joint angle with a sinusoidal trajectory at a series of five increasing frequencies with twenty cycles per frequency. We repeated this test at three different amplitudes (i.e., $\theta_{\rm j} = a \sin(2\pi f t), \forall f \in \{1, 2, 3, 4, 5\}$ Hz, $a \in \{0.035, 0.070, 0.105\}$ rad) and recorded the reaction torque produced by the ankle joint. We filtered the torque and angle data with a 4th order butterworth lowpass filter with a 15-Hz cutoff frequency.

2) Results—Joint Impedance Accuracy: To quantify each controller's ability to produce the desired impedance behaviors,

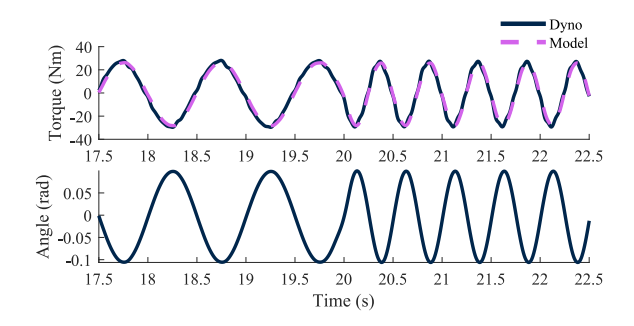


Fig. 6. Plots of the measured torque and joint angle for a 5s subsection of a constant-impedance experiment trial with our proposed controller C_1 . In this trial, $K_d=300.0$ Nm/rad and $B_d=5.0$ Nms/rad. The pink dashed line shows the predicted torque from the best fit second-order system.

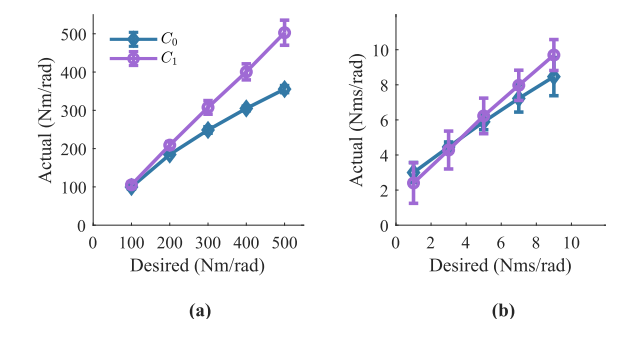


Fig. 7. Plots of the observed (a) joint stiffness \hat{K} and (b) joint damping \hat{B} as functions of desired values for the constant-impedance experiment. Solid lines connect the means at each desired point, and error bars indicate standard deviations. By compensating for the drivetrain dynamics (purple circles), the joint impedance rendered by C_1 is closer to the desired values than the impedance rendered by C_0 (blue diamonds).

we regressed each trial's torque and angle data to a linear model with inertia \hat{I} , viscous damping \hat{B} , and stiffness \hat{K} using least squares, i.e., $\hat{\tau}_{\rm j} = -\hat{K}\theta_{\rm j} - \hat{B}\dot{\theta}_{\rm j} - \hat{I}\ddot{\theta}_{\rm j}$, where $\hat{\tau}_{\rm j}$ is the predicted torque of the best-fit linear system (dashed line in Fig. 6). In general, the identified stiffness and damping parameters were closer to their desired values when using the proposed controller C_1 compared to the baseline C_0 (Fig. 7).

We also calculated the VAF of each linear model's predicted torque compared to the measured torque for each trial to measure goodness of fit. The mean VAF was 89.1% for the trials using C_0 and 88.6% for the trials using C_1 , suggesting that both systems, on average, behaved sufficiently like linear second-order systems.

Next, we empirically calculated the system's frequency response for each condition to check for frequency-dependent behaviors. We fit sinusoids to the measured torque data at each input amplitude and frequency and calculated the gain and phase shifts between the input and output. Fig. 8 shows an example of this frequency response for the trial with $K_d=300~\mathrm{Nm/rad}$ and $B_d=9.0~\mathrm{Nms/rad}$ averaged over each input amplitude. We calculated the frequency response error as the vector difference between the desired and output sinusoids viewed in the phasor plane, computed for each frequency. Across frequencies and magnitudes, the average frequency response error for C_1 was $33.1\pm40.2\%$, while the average error for C_0 was $55.7\pm28.3\%$.

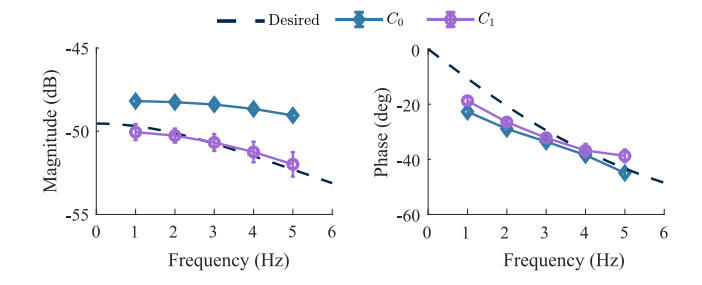


Fig. 8. Example frequency response plot of the observed and desired behavior for $K_d=300$ Nm/rad, $B_d=9$ Nms/rad averaged over the three tested amplitudes. Error bars (small) show one standard deviation.

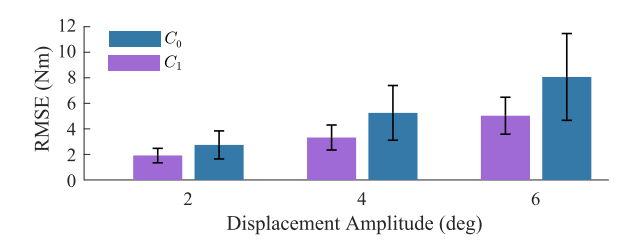


Fig. 9. RMS torque error as a function of joint angle amplitude averaged across all constant-impedance trials. The error was calculated relative to a system with the desired impedance subject to the same inputs. Error bars denote standard deviations. The proposed controller C_1 produced a significantly lower error (p < 0.05) than the baseline C_0 at each amplitude, indicating that its torque response was closer to that of the desired system.

Controller C_1 's reduction in the frequency response error compared to C_0 by 22.6% was statistically significant (p=0.026). To aid in interpreting these values, a transfer function with the correct gain but a 90° phase shift would result in 141% error.

Finally, we calculated the RMS error between the observed output torque and the output torque produced by a system with the desired impedance subjected to the same input. Shown in Fig. 9, the proposed controller C_1 produced a significantly lower torque error than the baseline controller C_0 for each amplitude (p < 0.05). On average, C_1 decreased the torque error by 1.9 Nm compared to C_0 .

3) Results—Torque Model Accuracy: In addition to the impedance accuracy, we evaluated the quality of the drivetrain model developed in Section III-A by comparing its output torque to the measured torque. Across all trials with both controllers, the drivetrain model's VAF was $96.3 \pm 2.7\%$. The RMS model error was 2.1 Nm, which equates to only 4.2% of the peak torque measured during the experiment (49.5 Nm). Therefore, the drivetrain model accurately predicted the output torque at the joint, regardless of the controller.

B. Variable-Impedance Experiments

1) Methods: While the first set of experiments investigated the OSL v2's ability to render a wide array of constant-impedance setpoints, it is also important to understand how the system behaves while rendering variable impedance trajectories, as humans are known to continuously modulate their joint impedance while walking [35], [36], [37], [38]. In this second experiment, we simulated walking kinematics using the

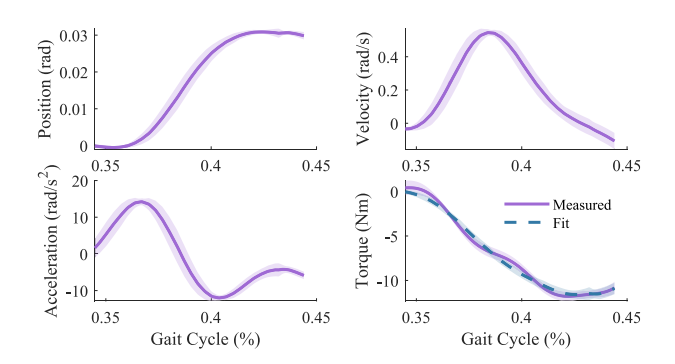


Fig. 10. Plots of the kinematic and kinetic deviation trajectories caused by the perturbation applied at 33% of the gait cycle: position (top left), velocity (top right), acceleration (bottom left) and torque (bottom right). Shaded regions represent ± 1 standard deviation about the mean. The dashed line on the torque plot shows the predicted torque of the best-fit linear system.

dynamometer and applied small, momentary joint perturbations at two different points during the gait cycle, analogous to the methods in [35] and [37]. We programmed the OSL v2 to replicate the biological ankle impedance trajectories reported in [37] scaled to a 70 kg person using the proposed controller C_1 . We calculated an equilibrium angle trajectory to replicate the normative ankle torque trajectories τ^* given the normative kinematics θ^* , $\dot{\theta}^*$ reported in [50]

$$\theta_{\rm eq} = \theta^* + \left(\tau^* + B_d \dot{\theta}^*\right) / K_d. \tag{22}$$

During each trial, the dynamometer moved the the joint through normative ankle kinematics for walking based on [50] at a cadence of eighty steps/min and recorded the reaction torque produced by the OSL v2. Thirty gait cycles were performed, with half of the trials including a momentary 0.035 rad perturbation superimposed on the kinematics for 200 ms at a specific timing point. The timing point was at approximately 11% of the gait cycle for the first batch of trials and 33% of the gait cycle for the second batch.

To estimate the joint impedance, we first calculated the average nominal position, velocity, acceleration (i.e., kinematic) and torque (i.e., kinetic) trajectories using the nonperturbed gait cycles. Then, we subtracted these nominal trajectories from the kinematic and kinetic data from each perturbed gait cycle, yielding a set of fifteen kinematic and kinetic deviation trajectories for each timing point. We isolated the first 150 ms following the perturbation onset for analysis (Fig. 10).

2) Results—Joint Impedance Accuracy: We regressed a second-order linear model to each deviation trajectory, yielding estimated stiffness, damping, and inertia parameter distributions. The dashed line in Fig. 10 shows the average torque predicted by the best-fit models for the second timing point. The VAF of the best-fit linear system was $70.3\pm19.4\%$ for the first timing point and $98.0\pm1.1\%$ for the second timing point. The mean observed stiffness and damping values during the analysis windows were similar to the desired values, particularly for stiffness (Fig. 11). While there was some deviation between the observed and desired damping values, the desired values were consistent with the distribution means (i.e., they were contained

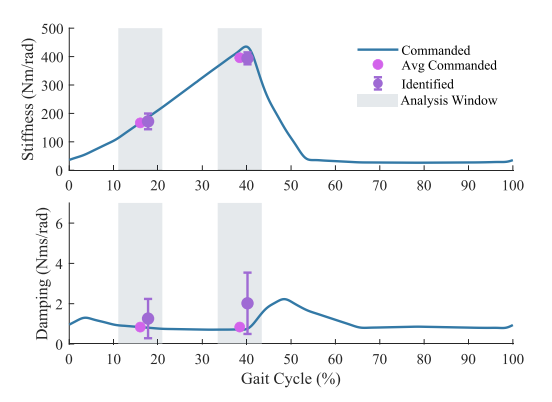


Fig. 11. Plots of the mean identified joint stiffness and damping at each timing point (purple), where each analysis window is shaded. The error bars denote one standard deviation about the mean. The blue line denotes the commanded able-bodied ankle impedance trajectories (reported in [38]), with pink markers indicating the mean commanded value during the analysis window.

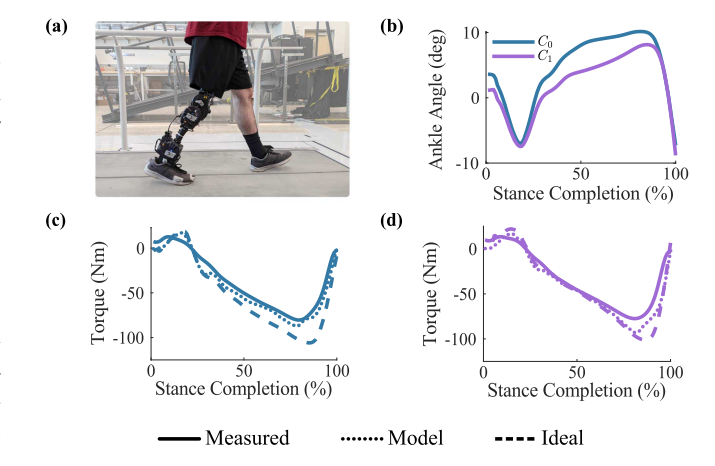


Fig. 12. (a) Photo of the participant with above-knee amputation walking on a treadmill using the OSL v2. (b) Mean ankle walking kinematics for each controller. (c) and (d) The mean ankle walking kinetics for controllers C_0 and C_1 , respectively, calculated via inverse dynamics (solid lines). Given the observed kinematics and the reference impedance trajectories, the desired joint torque (dashed) for each controller is also shown. Finally, the estimated joint torque given by the drivetrain model is shown (dotted).

in the 68% confidence intervals for the standard error of the mean).

3) Results—Torque Model Accuracy: We again evaluated the torque model for its ability to predict the torques measured in this simulated walking experiment, which encountered higher torques and larger motions than the constant-impedance experiments. During this experiment, the average nonperturbed peak torque per stride was 98.4 ± 0.8 Nm and the ankle range of motion was 0.417 ± 0.002 rad. The torque model's mean VAF was $97.7\pm0.2\%$ averaged across all trials. The RMS model error was 6.0 ± 0.2 Nm, which equates to only 6.1% of the peak experiment torque.

C. Treadmill Walking Experiments

1) Methods: In a final experiment, a participant with an above-knee amputation [Fig. 12(a)] walked on the OSL v2 on

a treadmill at 1 m/s using each low-level impedance controller. The experimental protocol was approved by the Institutional Review Board of the University of Michigan (HUM00143080). We implemented the phase-based walking controller from [22], which provided reference stance-phase impedance trajectories. Motion capture recordings along with forceplate and encoder measurements were used to calculate the OSL v2's ankle kinematics and kinetics [Fig. 12(b) and (c)].

2) Results: The participant was able to walk comfortably using both controllers, with each producing natural gaits [Fig. 12(a)]. Unlike the first experiments, in which the dynamometer regulated the joint position, both the kinematics and kinetics in this experiment were free to vary based on the dynamic interaction between the user and the ground. Qualitatively, we note that the uncompensated controller C_0 produced a larger stance-phase range of motion than the proposed controller C_1 . We hypothesize that the user created this extra deflection instinctively in order to achieve sufficient joint torque to initiate pushoff, as the torque trajectories of each controller are similar [Fig. 12(c) and (d)].

As impedance control aims to regulate the joint's dynamics, we evaluate our controller on its ability to create the correct torque response given the observed kinematics. Importantly, we do not evaluate kinematic or kinetic similarity to a reference (e.g., able-bodied), as this is not the explicit objective an impedance controller. Inputting the observed kinematics and the reference K, B, and $\theta_{\rm eq}$ into the impedance control law, we find that C_0 should have provided much more torque at this increased deflection [dashed in Fig. 12(c)]with mean absolute torque error (MAE) of 16.2 Nm. In contrast, controller C_1 's torque trajectory is close to the desired for the majority of the gait cycle with an MAE of 9.6 Nm, indicating more accurate joint impedance control during walking compared to C_0 .

Finally, despite the different controllers, the drivetrain model from Section III-A accurately predicted the true ankle torque from inverse dynamics [dotted line in Fig. 12(c)–(d)]. This agreement further validates the model's accuracy, and demonstrates its usefulness in real-world walking scenarios.

V. DISCUSSION

The OSL v2 was designed to accelerate research in the control of robotic prostheses by providing an economical, versatile, and high-performance hardware platform. We believe a common hardware platform will enable the academic community to more rapidly innovate and share ideas, ultimately quickening the pace of translation. A key feature in a high-performance prosthesis is the ability to accurately control joint mechanical impedance. Due to the system's inherent inertial, dissipative, and elastic dynamics, uncompensated open-loop control strategies are inadequate to achieve this requirement. In this work, we proposed an actuator-state feedback controller, which we developed around a simple, analytical model of the system's dynamics. We implemented the controller on the OSL v2 ankle joint and demonstrated substantial improvements in the impedance accuracy compared to a baseline, uncompensated controller. Our control

approach is generalizable and relevant to hardware systems that include intentional or unintentional series elasticity.

A. Joint Impedance Accuracy

In the constant impedance experiment, the identified stiffness and damping for our proposed controller C_1 were closer to the desired values when compared to the baseline controller C_0 (Fig. 7). This improvement is particularly true for stiffness, as controller C_0 was unable to effectively render higher stiffness values, likely because C_0 ignores the compliance of the belt transmission; an additional series compliance always reduces the effective stiffness. Damping was slightly improved by controller C_1 , but both controllers were unable to make the system render very low damping values. The mean fit quality across both controllers was relatively high (88.9% VAF), indicating that the identified stiffness and damping values are representative of the system's true dynamics.

We also investigated the effects of varying the input frequency on each controller's performance. Controller C_1 showed a significantly lower mean frequency response error compared to C_0 , indicating that its torque output across the frequency domain was closer to the desired system (see, e.g., Fig. 8). We observe similar results in the RMS torque error plot (Fig. 9), where controller C_1 produced a torque output that was on average closer to the torque of the desired system compared to C_0 . While the RMS error for both controllers increased with increasing amplitude (and thus increasing joint torques), C_0 's errors increased faster than C_1 's. In aggregate, these results suggest that: 1) compensating for the drivetrain dynamics is important; and 2) the described control method is effective at reducing the impacts of these dynamics on the rendered impedance behavior.

We further demonstrated the proposed controller C_1 's efficacy in the simulated walking experiments with variable impedance trajectories. This experiment tested the joint impedance at two timing points with different desired stiffness coefficients. Controller C_1 was able to produce the desired joint stiffness at both timing points (Fig. 11), indicating our approach can track a variable stiffness trajectory while simultaneously creating the substantial torques required for walking (98 Nm peak). The joint's damping was not as accurately rendered, and the results were consistent with those found in the constant-impedance experiments (Fig. 7), which show that low damping values are difficult for both controllers.

The final experiment demonstrated the proposed controller's utility in a real walking task on a treadmill, and its improved performance relative to the uncompensated alternative. By factoring in the transmission elasticity, controller C_1 much more closely tracked the ankle torque given by the desired joint impedance compared to C_0 [Fig. 12(c)]. Because C_0 did not account for the additional joint motion provided by the transmission elasticity, the participant had to create extra ankle dorsiflexion in order to produce sufficient torque for pushoff. Future work could study the biomechanical benefits of C_1 with more subjects and more thorough measurements (e.g., inverse dynamics, surface electromyography, metabolic cost, etc.).

While modern impedance controllers have been shown to produce biomimetic kinematics and kinetics during various locomotion activities [22], [51], [52], [53], [54], [55], their impedance (i.e., their response to disturbances) is not necessarily biomimetic. These experiments show that the OSL v2 could be used with controller C_1 to render an impedance controller that is biomimetic with respect to both joint impedance *and* kinematics and kinetics, which may show interesting biomechancial advantages stemming from the human-like dynamics.

Finally, our proposed controller could likely be applicable to systems beyond the OSL v2. The drivetrain model (Fig. 4) is sufficiently general to describe the dynamics of many other prostheses with compliance in their transmissions. This compliance could be intentional, such as in the case of SEAs, or unintentional, such as belt, gear, or frame elasticity.

B. Torque Model Accuracy

We evaluated the accuracy of the torque model (Section III-A, Fig. 4) with the data from both experiments and found that the model accurately predicted the joint torque. The model's RMS error was 6.1% of the peak torque or lower in both experiments, with VAF values of 96% or better. The experiments included wide ranges of motor currents, joint angles, velocities, and accelerations, suggesting that model's accuracy would hold broadly across operating regimes. The high accuracy of the torque model means that it could potentially be used in many helpful applications, including torque control, inverse dynamics, and additional data for higher-level control strategies. Finally, the results from this study can be directly applied by other researchers that use the OSL v2, potentially enabling a reduction in the required equipment and protocol complexity.

C. Limitations

While the experiments highlighted the efficacy of our proposed controller, there are various limitations to our approach that should be noted. First, our dynamic model (Fig. 4) is a simplification of the true system dynamics, and some of the features it ignores may impact the controller's performance. For example, the torque-angle behavior of the transmission is not as smooth as the quadratic model assumes (Fig. 3), and the backlash around zero deflection may be important to consider during low-torque conditions.

In addition, the experiments showed that the damping regulation of our controller is not as accurate as the stiffness regulation. Although we pick the value of B_1 that minimizes the frequency response error, it does not guarantee that the error is zero. Fundamentally, this error will always be nonzero because the closed-loop transfer function (19) has two extra zeros and one extra pole compared to the desired single pole system. Therefore, frequency response of the actual system will always deviate from the desired at some frequencies, regardless of gain selection. For the human ankle joint, however, the stiffness component constitutes a much larger portion of the perturbation torque response than the damping component [37], [38], perhaps limiting the consequence of this limitation.

An alternative one could use to avoid this issue is to also include additional feedback using the belt deflection states ($\theta_{\rm s}$ and $\dot{\theta}_{\rm s}$) in (8), which would allow cancellation or arbitrary placement of the closed-loop poles and zeros (i.e., using a full-state-feedback controller) [47]. However, this approach requires very accurate measurements of $\theta_{\rm s}$ and $\dot{\theta}_{\rm s}$ in practice. The minor backlash displayed in Fig. 3 suggests that stability would be a concern when applying a full-state-feedback controller to our system.

There are also design options one could use to make the system easier to control, such as reducing the actuator inertia. A lower value of $J_{\rm a}$ would push the transfer function's zeros further into the left-half plane, delaying their effect until higher frequencies and allowing our controller to better produce the desired damping at walking frequencies. Reducing the gear ratios $n_{\rm t}$ and $n_{\rm a}$ would have similar effects, but at the expense of reduced torque capacity. These tradeoffs were considered during the OSL v2 design process, and maintaining sufficient peak torque was ultimately selected as a priority.

There are also practical limitations to our proposed controller. Like other model-based methods, our controller requires accurate values for the system parameters, such as the inertial and friction properties of the actuator and the belt deflection characteristics. While in theory these properties should not vary with time, this has not yet been investigated. Future work should investigate the variance of the model parameters and the controller's sensitivity to them.

VI. CONCLUSION

In this article, we presented a novel joint impedance controller for prostheses with significant inertial, dissipative, and elastic drivetrains, and we evaluated the controller experimentally on the second-generation Open-Source Leg. First, we detailed the design updates made in the OSL v2 revision, which resulted in an easy to use, capable, and affordable research platform. We then characterized the new system's dynamics and showed that they can be well explained via a simple analytical model. We demonstrated that our model can accurately predict the OSL v2 output torque across diverse conditions. Using this model, we developed our controller based on feedback linearization and actuator-state feedback control, and we experimentally demonstrated its improved impedance accuracy compared to a baseline controller. We further showed our controller's ability to track the variable impedance trajectories of the human ankle joint during walking, indicating that our controller could be used with the OSL v2 to create highly biomimetic behavior.

APPENDIX

A. Derivations of Selected Expressions

1) Friction Compensation: We desire linearized actuator dynamics of the form

$$\tau_{\rm a} = \tau_{\rm a}^{\rm des} - B_{\rm a}\dot{\theta}_{\rm a} - J_{\rm a}\ddot{\theta}_{\rm a}. \tag{23}$$

Equating the desired dynamics with the actuator's true dynamics (1) yields an expression relating $\tau_{\rm a}^{\rm des},\dot{\theta}_{\rm a},$ and I_q

$$\tau_{\mathbf{a}}^{\text{des}} = I_q k_t n_{\mathbf{a}} - \operatorname{sgn}(\dot{\theta}_{\mathbf{a}}) (f_c + f_g | I_q |). \tag{24}$$

Two useful properties of the sgn(x) function are

$$|x| = \operatorname{sgn}(x)x,\tag{25}$$

$$sgn(xy) = sgn(x)sgn(y). (26)$$

Thus using (25), we can rewrite (24) as

$$\tau_{\mathbf{a}}^{\mathsf{des}} + \mathsf{sgn}(\dot{\theta}_{\mathbf{a}}) f_c = I_q(k_t n_{\mathbf{a}} - \mathsf{sgn}(I_q) \mathsf{sgn}(\dot{\theta}_{\mathbf{a}}) f_g). \tag{27}$$

We note that given our identified model parameters, $k_t n_{\rm a} - {\rm sgn}(I_q) {\rm sgn}(\dot{\theta}_{\rm a}) f_g > 0 \ \forall \ \dot{\theta}_{\rm a}, I_q \in \mathbb{R}$. This implies that ${\rm sgn}(\tau_{\rm a}^{\rm des} + {\rm sgn}(\dot{\theta}_{\rm a}) f_c) = {\rm sgn}(I_q)$. If we substitute this relationship back into (27), we find

$$\tau_{\rm a}^{\rm des} + {\rm sgn}(\dot{\theta}_{\rm a}) f_c = I_q(k_t n_{\rm a} -$$

$$\operatorname{sgn}(\tau_{\mathrm{a}}^{\mathrm{des}} + \operatorname{sgn}(\dot{\theta}_{\mathrm{a}}) f_c) \operatorname{sgn}(\dot{\theta}_{\mathrm{a}}) f_g).$$
 (28)

Distributing the $sgn(\theta_a)$ term via (26) and again using (25) to consolidate terms, we find

$$\tau_{\mathbf{a}}^{\mathsf{des}} + \mathsf{sgn}(\dot{\theta}_{\mathbf{a}}) f_c = I_q \left(k_t n_{\mathbf{a}} - \mathsf{sgn}(\tau_{\mathbf{a}}^{\mathsf{des}} \dot{\theta}_{\mathbf{a}} + |\dot{\theta}_{\mathbf{a}}| f_c) f_g \right). \tag{29}$$

From here, simply rearranging terms produces (6).

2) Bias Angle: To calculate θ_a^* , we begin by equating the desired and actual steady state joint torques and substituting in the identified gain K_1

$$-K_d\theta_{j} = -n_t K_1(\theta_a - \theta_a^*), \tag{30}$$

$$\theta_{\rm j} = \frac{K_{\rm s}}{n_{\rm t}(K_{\rm s} - K_d)} \left(\theta_{\rm a} - \theta_{\rm a}^*\right). \tag{31}$$

Next, we substitute for θ_a in terms of θ_s and θ_i using (3)

$$\theta_{\rm j} = \frac{K_{\rm s}}{(K_{\rm s} - K_d)} \left((\theta_{\rm j} - \theta_{\rm s}) - \frac{\theta_{\rm a}^*}{n_{\rm t}} \right). \tag{32}$$

Then, we substitute our approximation for deflection angle in terms of the local belt stiffness (12)

$$\theta_{j} = \frac{K_{s}}{(K_{s} - K_{d})} \left(\theta_{j} - \rho^{-1}(\tau_{0}) + \frac{-K_{d}\theta_{j} - \tau_{0}}{-K_{s}} - \frac{\theta_{a}^{*}}{n_{t}} \right).$$
(33)

Rearranging terms produces

$$\theta_{\rm j} \left(\frac{K_{\rm s} - K_d}{K_{\rm s}} - 1 + \frac{K_d}{K_{\rm s}} \right) = -\rho^{-1}(\tau_0) - \frac{\tau_0}{-K_{\rm s}} - \frac{\theta_{\rm a}^*}{n_{\rm t}}.$$
 (34)

Noting that

$$\left(\frac{K_{\rm s} - K_d}{K_{\rm s}} - 1 + \frac{K_d}{K_{\rm s}}\right) = 0\tag{35}$$

the terms in (34) can be rearranged to produce (17).

ACKNOWLEDGMENT

The authors would like to thank Mr. Maurice Miro for design efforts on the OSL v2, Mr. Jace Derosia for his contributions to the OSL v2 software library, Mr. Nikko Van Crey for his assistance with the rotary dynamometer, Ms. Ellie Wilson for motion capture assistance, and our participant for making this work possible. They would also like to thank Goengineer and the

SOLIDWORKS for Good program for their generous software support.

REFERENCES

- S. M. Jaegers, J. H. Arendzen, and H. J. D. Jongh, "Prosthetic gait of unilateral transfemoral amputees: A kinematic study," *Arch. Phys. Med. Rehabil.*, vol. 76, no. 8, pp. 736–743, 1995.
- [2] N. Steinberg, A. Gottlieb, I. Siev-Ner, and M. Plotnik, "Fall incidence and associated risk factors among people with a lower limb amputation during various stages of recovery—A systematic review," *Disabil. Rehabil.*, vol. 41, no. 15, pp. 1778–1787, 2019.
- [3] D. M. Ehde, D. G. Smith, J. M. Czerniecki, K. M. Campbell, D. M. Malchow, and L. R. Robinson, "Back pain as a secondary disability in persons with lower limb amputations," *Arch. Phys. Med. Rehabil.*, vol. 82, no. 6, pp. 731–734, 2001.
- [4] D. C. Norvell, J. M. Czerniecki, G. E. Reiber, C. Maynard, J. A. Pecoraro, and N. S. Weiss, "The prevalence of knee pain and symptomatic knee osteoarthritis among veteran traumatic amputees and nonamputees," *Arch. Phys. Med. Rehabil.*, vol. 86, no. 3, pp. 487–493, 2005.
- [5] J. Keeves, A. Hutchison, K. D'Cruz, and S. Anderson, "Social and community participation following traumatic lower limb amputation: An exploratory qualitative study," *Disabil. Rehabil.*, vol. 45, no. 26, pp. 4404–4412, 2022.
- [6] B. J. Hafner and R. L. Askew, "Physical performance and self-report outcomes associated with use of passive, adaptive, and active prosthetic knees in persons with unilateral, transfemoral amputation: Randomized crossover trial," J. Rehabil. Res. Dev., vol. 52, no. 6, pp. 677–700, 2015.
- [7] D. A. Winter, "Energy generation and absorption at the ankle and knee during fast, natural, and slow cadences," *Clin. Orthopaedics Related Res.*, vol. 175, pp. 147–154, 1983.
- [8] P. DeVita, J. Helseth, and T. Hortobagyi, "Muscles do more positive than negative work in human locomotion," *J. Exp. Biol.*, vol. 210, no. 19, pp. 3361–3373, 2007.
- [9] M. R. Tucker et al., "Control strategies for active lower extremity prosthetics and orthotics: A review," *J. Neuroeng. Rehabil.*, vol. 12, no. 1, pp. 1–29, 2015.
- [10] R. R. Torrealba and E. D. Fonseca-Rojas, "Toward the development of knee prostheses: Review of current active devices," *Appl. Mech. Rev.*, vol. 71, no. 3, pp. 1–22, 2019.
- [11] R. Gehlhar, M. Tucker, A. J. Young, and A. D. Ames, "A review of current state-of-the-art control methods for lower-limb powered prostheses," *Annu. Rev. Control.*, vol. 55, pp. 142–164, 2023.
- [12] A. F. Azocar, L. M. Mooney, J. F. Duval, A. M. Simon, L. J. Hargrove, and E. J. Rouse, "Design and clinical implementation of an open-source bionic leg," *Nat. Biomed. Eng.*, vol. 4, no. 10, pp. 941–953, 2020.
- [13] S. Ayyappan, "The open source leg," 2023. [Online]. Available: https://www.opensourceleg.org/build
- [14] F. Sup, H. Varol, J. Mitchell, T. Withrow, and M. Goldfarb, "Self-contained powered knee and ankle prosthesis: Initial evaluation on a transfemoral amputee," in *Proc. IEEE Int. Conf. Rehabil. Robot.*, 2009, pp. 638–644.
- [15] F. Sup, H. A. Varol, and M. Goldfarb, "Upslope walking with a powered knee and ankle prosthesis: Initial results with an amputee subject," *IEEE Trans. Neural Syst. Rehabil. Eng.*, vol. 19, no. 1, pp. 71–78, Feb. 2011.
- [16] A. Bayen et al., "Realization of nonlinear real-time optimization based controllers on self-contained transfemoral prosthesis," in *Proc. ACM/IEEE Int. Conf. Cyber-Phys. Syst.*, 2015, pp. 130–138.
- [17] L. Gabert, S. Hood, M. Tran, M. Cempini, and T. Lenzi, "A compact, lightweight robotic ankle-foot prosthesis: Featuring a powered polycentric design," *IEEE Robot. Autom. Mag.*, vol. 27, no. 1, pp. 87–102, Mar. 2020.
- [18] T. Elery, S. Rezazadeh, C. Nesler, and R. D. Gregg, "Design and validation of a powered knee-ankle prosthesis with high-torque, low-impedance actuators," *IEEE Trans. Robot.*, vol. 36, no. 6, pp. 1649–1668, Dec. 2020.
- [19] N. Anil Kumar, S. Patrick, W. Hong, and P. Hur, "Control framework for sloped walking with a powered transfemoral prosthesis," *Front. Neuro*robot., vol. 15, pp. 1–12, 2022.
- [20] M. Kim, A. M. Simon, and L. J. Hargrove, "Seamless and intuitive control of a powered prosthetic leg using deep neural network for transfemoral amputees," Wear. Tech., vol. 3, 2022, Art. no. e24.
- [21] S. Hood, L. Gabert, and T. Lenzi, "Powered knee and ankle prosthesis with adaptive control enables climbing stairs with different stair heights, cadences, and gait patterns," *IEEE Trans. Robot.*, vol. 38, pp. 1430–1441, Jun. 2022.

- [22] T. K. Best, C. G. Welker, E. J. Rouse, and R. D. Gregg, "Data-driven variable impedance control of a powered knee–ankle prosthesis for adaptive speed and incline walking," *IEEE Trans. Robot.*, vol. 39, no. 3, pp. 2151–2169, Jun. 2023.
- [23] G. Fu, J. Zhu, Z. Wang, J. Mai, Q. Wang, and Q. Wang, "Mechatronic design and implementation of a low-noise powered knee prosthesis with high backdrivability," *IEEE ASME Trans. Mechatron.*, vol. 28, no. 6, pp. 3180–3190, Dec. 2023.
- [24] B. E. Lawson, J. Mitchell, D. Truex, A. Shultz, E. Ledoux, and M. Goldfarb, "A robotic leg prosthesis: Design, control, and implementation," *IEEE Robot. Autom. Mag.*, vol. 21, no. 4, pp. 70–81, Dec. 2014.
- [25] E. J. Rouse, L. M. Mooney, and H. M. Herr, "Clutchable series-elastic actuator: Implications for prosthetic knee design," *Int. J. Robot. Res.*, vol. 33, pp. 1611–1625, 2014.
- [26] R. R. Posh, J. P. Schmiedeler, and P. M. Wensing, "Finite-state impedance and direct myoelectric control for robotic ankle prostheses: Comparing their performance and exploring their combination," *IEEE Trans. Neural* Syst. Rehabil. Eng., vol. 31, pp. 2778–2788, 2023.
- [27] A. F. Azocar and E. J. Rouse, "Characterization of open-loop impedance control and efficiency in wearable robots," *IEEE Robot. Autom. Lett.*, vol. 7, no. 2, pp. 4313–4320, Apr. 2022.
- [28] S. K. Au, J. Weber, and H. Herr, "Powered ankle—Foot prosthesis improves walking metabolic economy," *IEEE Trans. Robot.*, vol. 25, no. 1, pp. 51–66, Feb. 2009.
- [29] J. K. Hitt, T. G. Sugar, M. Holgate, and R. Bellman, "An active foot-ankle prosthesis with biomechanical energy regeneration," *J. Med. Device.*, vol. 4, no. 1, 2010, Art. no. 011003.
- [30] J. M. Caputo and S. H. Collins, "A universal ankle–Foot prosthesis emulator for human locomotion experiments," *J. Biomech. Eng.*, vol. 136, no. 3, 2014, Art. no. 035002.
- [31] W. F. Rampeltshammer, A. Q. L. Keemink, and H. V. D. Kooij, "An improved force controller with low and passive apparent impedance for series elastic actuators," *IEEE ASME Trans. Mechatron.*, vol. 25, no. 3, pp. 1220–1230, Jun. 2020.
- [32] G. Aguirre-Ollinger, J. E. Colgate, M. A. Peshkin, and A. Goswami, "Design of an active one-degree-of-freedom lower-limb exoskeleton with inertia compensation," *Int. J. Robot. Res.*, vol. 30, no. 4, pp. 486–499, 2011
- [33] D. Quintero, D. J. Villarreal, D. J. Lambert, S. Kapp, and R. D. Gregg, "Continuous-phase control of a powered knee-ankle prosthesis: Amputee experiments across speeds and inclines," *IEEE Trans. Robot.*, vol. 34, no. 3, pp. 686–701, Jun. 2018.
- [34] T. Lenzi, M. Cempini, L. Hargrove, and T. Kuiken, "Design, development, and testing of a lightweight hybrid robotic knee prosthesis," *Int. J. Rob. Res.*, vol. 37, pp. 953–976, 2018.
- [35] E. Rouse, L. Hargrove, E. Perreault, and T. Kuiken, "Estimation of human ankle impedance during the stance phase of walking," *IEEE Trans. Neural Syst. Rehabil. Eng.*, vol. 22, no. 4, pp. 870–878, Jul. 2014.
- [36] H. Lee and N. Hogan, "Time-varying ankle mechanical impedance during human locomotion," *IEEE Trans. Neural Syst. Rehabil. Eng.*, vol. 23, no. 5, pp. 755–764, Sep. 2015.
- [37] A. L. Shorter and E. J. Rouse, "Mechanical impedance of the ankle during the terminal stance phase of walking," *IEEE Trans. Neural Syst. Rehabil. Eng.*, vol. 26, no. 1, pp. 135–143, Jan. 2018.
- [38] H. Lee, E. J. Rouse, and H. I. Krebs, "Summary of human ankle mechanical impedance during walking," *IEEE J. Transl. Eng. Health Med.*, vol. 4, 2016, Art. no. 2100407.
- [39] N. E. Krausz and L. J. Hargrove, "Sensor fusion of vision, kinetics, and kinematics for forward prediction during walking with a transfemoral prosthesis," *IEEE Trans. Med. Robot. Bionics*, vol. 3, no. 3, pp. 813–824, Aug. 2021.
- [40] S. B. Finucane, L. J. Hargrove, and A. M. Simon, "Functional mobility training with a powered knee and ankle prosthesis," *Front. Rehabil. Sci.*, vol. 3, 2022, Art. no. 790538.
- [41] J. Camargo, K. Bhakta, J. Maldonado-Contreras, S. Zhou, K. Herrin, and A. Young, "Opensim model for biomechanical analysis with the opensource bionic leg," in *Proc. 2022 Int. Symp. Med. Robot.*, 2022, pp. 1–6.
- [42] T. Thomas and A. Kurian, "Robotic technology in the development of prosthesis," in *Machine Learning for Critical Internet of Medical Things*, Cham, Switzerland: Springer, 2022, pp. 153–175.
- [43] A. F. Azocar, L. M. Mooney, L. J. Hargrove, and E. J. Rouse, "Design and characterization of an open-source robotic leg prosthesis," in *Proc. IEEE RAS EMBS Int. Conf. Biomed. Robot. Biomechatronics*, 2018, pp. 111–118.

- [44] C. Nesler, G. Thomas, N. Divekar, E. J. Rouse, and R. D. Gregg, "Enhancing voluntary motion with modular, backdrivable, powered hip and knee orthoses," *IEEE Robot. Autom. Lett.*, vol. 7, no. 3, pp. 6155–6162, Jul. 2022.
- [45] U. H. Lee, C.-W. Pan, and E. J. Rouse, "Empirical characterization of a high-performance exterior-rotor type brushless DC motor and drive," in *Proc. IEEE/RSJ Int. Conf. Intell. Robots Syst.*, 2019, pp. 8018–8025.
- [46] M. W. Spong, "Modeling and control of elastic joint robots," J. Dyn. Syst. Meas. Control, vol. 109, no. 4, pp. 310–318, 1987.
- [47] A. Albu-Schaffer and G. Hirzinger, "State feedback controller for flexible joint robots: A globally stable approach implemented on DLR's lightweight robots," in *Proc. IEEE/RSJ Int. Conf. Intell. Robots Syst.*, 2000, pp. 1087–1093.
- [48] M. W. Spong, S. Hutchinson, and M. Vidyasagar, Robot Modeling and Control (2nd ed.). Hoboken, NJ, USA: Wiley, 2020.
- [49] G. C. Thomas, J. S. Mehling, J. Holley, and L. Sentis, "Phase-relaxed-Passive full state feedback gain limits for series elastic actuators," *IEEE ASME Trans. Mechatron.*, vol. 26, no. 1, pp. 586–591, Feb. 2021.
- [50] E. Reznick, K. R. Embry, R. Neuman, E. Bolívar-Nieto, N. P. Fey, and R. D. Gregg, "Lower-limb kinematics and kinetics during continuously varying human locomotion," *Sci. Data*, vol. 8, 2021, Art. no. 282.
- [51] M. F. Eilenberg, H. Geyer, and H. Herr, "Control of a powered ankle-foot prosthesis based on a neuromuscular model," *IEEE Trans. Neural Syst. Rehabil. Eng.*, vol. 18, no. 2, pp. 164–173, Apr. 2010.
- [52] A. M. Simon et al., "Configuring a powered knee and ankle prosthesis for transfemoral amputees within five specific ambulation modes," *PLoS One*, vol. 9, no. 6, 2014, Art. no. e99387.
- [53] A. H. Shultz and M. Goldfarb, "A unified controller for walking on even and uneven terrain with a powered ankle prosthesis," *IEEE Trans. Neural* Syst. Rehabil. Eng., vol. 26, no. 4, pp. 788–797, Apr. 2018.
- [54] C. G. Welker, T. K. Best, R. D. Gregg, and C. G. Welker, "Improving sit/stand loading symmetry and timing through unified variable impedance control of a powered knee-ankle prosthesis," *IEEE Trans. Neural Syst. Rehabil. Eng.*, vol. 31, pp. 4146–4155, 2023.
- [55] R. J. Cortino, T. K. Best, and R. D. Gregg, "Data-driven phase-based control of a powered knee-ankle prosthesis for variable-incline stair ascent and descent," *IEEE Trans. Med. Robot. Bionics*, vol. 6, no. 1, pp. 175–188, Feb. 2024.



T. Kevin Best (Student Member, IEEE) received the B.S. degree in mechanical engineering from the University of Notre Dame, South Bend, IN, USA, in 2018, and the M.S. degree in robotics, in 2022, from the University of Michigan, Ann Arbor, MI, USA, where he is currently a doctoral candidate with the Locomotor Control Systems Laboratory and the Neurobionics Laboratory, Department of Robotics.

His research interests include control of robotic systems, optimization, and biomechanics.



Gray C. Thomas (Member, IEEE) received the B.S. degree in engineering: robotics with the Olin College of Engineering, Needham, MA, USA, in 2012, and the Ph.D. degree in mechanical engineering from the University of Texas at Austin, Austin, TX, USA, in 2019.

He is currently an Assistant Professor with the Department of Mechanical Engineering, Texas A&M University, College Station, TX. He worked on the topics of multicontact impedance control for humanoid robots, system identification for

robust control, and series elastic actuation at the University of Texas at Austin. He studies direct human control of physically interactive robots through a combination of strength amplification control, human modeling and estimation, and high-bandwidth design. His other research interests include force-feedback, series-elastic actuation, and robust control

Dr. Thomas was the recipient of the NASA Space Technology Research Fellowship and Olin Full-Tuition Scholarship.



Senthur R. Ayyappan received the B.Tech. degree in production engineering from the National Institute of Technology Tiruchirappalli, India, in 2020.

He is currently a Research Engineer with the Neurobionics Laboratory, Department of Robotics, University of Michigan, Ann Arbor, MI, USA. His research interests include bio-inspired design, computational and generative design, and community-driven development.



Robert D. Gregg (Senior Member, IEEE) received the B.S. degree in electrical engineering and computer sciences from the University of California at Berkeley, Berkeley, CA, USA, in 2006, and the M.S. and Ph.D. degrees in electrical and computer engineering from the University of Illinois at Urbana-Champaign, Champaign, IL, USA, in 2007 and 2010, respectively.

He was previously an Assistant Professor with The University of Texas at Dallas, Richardson, TX, USA. In 2019, he joined the Department

of Electrical Engineering and Computer Science, University of Michigan, Ann Arbor, MI, USA, as an Associate Professor. He joined the Department of Robotics, University of Michigan, in 2022. His research interests include the control of bipedal locomotion with applications to autonomous and wearable robots.



Elliott J. Rouse (Senior Member, IEEE) received the B.S. degree in mechanical engineering from The Ohio State University, Columbus, OH, USA, in 2007, and the M.S. and Ph.D. degrees in biomedical engineering from Northwestern University, Evanston, IL, USA, in 2009 and 2012, respectively.

Afterwards, he joined the Massachusetts Institute of Technology, Cambridge MA, USA, as a Postdoctoral Fellow until 2014. He is currently an Associate Professor with the Departments

of Robotics and Mechanical Engineering, University of Michigan, Ann Arbor, MI, USA. Prior to joining the University of Michigan, he was Faculty with the Shirley Ryan AbilityLab / Northwestern University, Chicago, IL, USA; from 2020 to 2021, he was a Visiting Faculty Member with (Google) X, Mountain View, CA, USA. His research interests include precision machine design, control, biomechanical modeling, psychophysics, and the use of these tools to develop meaningful exoskeletons and robotic prostheses that advance gait, mobility, and quality of life